Int. J. Heat Mass Transfer. Vol. 31, No. 10, pp. 2077–2089, 1988
Printed in Great Britain

0017–9310/88 $3.00+0.00

Double-diffusive convection due to melting

C. BECKERMANN and R. VISKANTA
Heat Transfer Laboratory, School of Mechanical Engineering, Purdue University, West Lafayette, IN 47907, U.S.A.

(*Received* 9 *November* 1987 *and in final form* 15 *March* 1988)

Abstract—A combined numerical and experimental study is reported of melting of a vertical ice layer into an ammonium chloride–water solution inside a square cavity. The governing equations are solved utilizing an algorithm which is based on curvilinear, non-orthogonal control volumes. The numerical results are successfully validated through shadowgraph, flow visualization, temperature and concentration measurements. It is found that the melting process induces temperature and concentration gradients in the initially homogeneous liquid. Due to the double-diffusive nature of the system, this results in the development of a stable concentration stratification above a layer of strongly convecting, uncontaminated liquid. It is conclusively shown that the double-diffusive convection processes cause considerable variations in the local melting rates and the interfacial temperature and concentration distributions. The heat transfer rates at the vertical walls of the cavity and the heat conduction in the solid region strongly reflect the time evolution of the double-diffusive convection phenomena induced by the melting process.

1. INTRODUCTION

SOLID/liquid phase change in binary mixtures has recently received increased research attention due to its large range of applications, including solidification of castings [1], crystal growth [2], magmatic crystallization [3–5], melting of icebergs in oceans [6], etc. It is now well recognized that natural convection has a profound influence on the melting and solidification processes as well as on the properties of the solidified materials [1–7]. During phase change of fluids consisting of more than a single chemical species, natural convection is caused by the simultaneous action of thermal and solutal driving forces. Since the latent heat must be transported to (solidification) or from (melting) the solid/liquid interface, temperature gradients develop in the liquid, which induce thermal natural convection. Concentration gradients exist in the liquid due to preferential incorporation or rejection of a species at the solid/liquid interface. These gradients cause solutal natural convection. The local temperature and concentration at the interface are directly related by the equilibrium phase diagram of a binary mixture. Hence, during phase change in binary mixtures, thermal and solutal natural convection will develop simultaneously. Because most binary fluids have vastly different molecular diffusivities for heat and species, such natural convection is often called double-diffusive convection [8, 9].

Double-diffusive convection during phase change in binary mixtures has been the subject of a number of recent investigations [1–9]. During both, melting and solidification in containers, complex convection patterns have been observed. Even in an initially homogeneous liquid, double-diffusive convection can be induced by the phase-change process itself [3, 4]. During melting and solidification along vertical boundaries, horizontal liquid layers of different composition can be formed which are separated by relatively thin interfaces [3–6]. The melting or solidification rates are substantially influenced by the different environments in these layers. In phase change from below or above, finger instabilities can be generated because of a destabilizing concentration gradient [4]. It has been shown that such double-diffusive fingers are the cause of 'freckles' in solidified alloy castings [7].

These are but a few examples of the importance of double-diffusive convection during melting and solidification of binary mixtures. Most of the previous studies are, however, qualitative in nature, and the two-dimensional, transient transport phenomena observed in such systems have not been predicted. Hence, it is the objective of the present study to develop a model of phase change in binary mixtures and to verify the model predictions through experiments. For this purpose, a relatively simple physical system is selected which consists of a rectangular cavity simultaneously occupied by vertical layers of ice and a binary aqueous solution (Fig. 1). The vertical side walls of the cavity are maintained at uniform temperatures such that the ice melts into the binary solution. The melting process induces compositional and thermal gradients in the initially homogeneous fluid. While this paper is limited to melting of ice into an aqueous solution, solidification of binary mixtures is considered in another study [10].

Melting of vertical ice layers into saline water has been investigated by oceanographers [6]. Their studies are motivated by melting of icebergs and glacial ice into the adjoining seas. Huppert and Turner [6] have recently reported an experimental study of melting of a vertical ice surface into a salinity gradient. Because of its lower salinity, the melt water is less dense than its surroundings and rises up the ice surface in a thin

NOMENCLATURE

A	aspect ratio, H/L
c	specific heat [J kg^{-1} K^{-1}]
C	concentration [kg kg^{-1}]
D	mass diffusivity [m^2 s^{-1}]
g	gravitational acceleration [m s^{-2}]
Δh	latent heat of fusion [J kg^{-1}]
H	height of enclosure [m]
k	thermal conductivity [W m^{-1} K^{-1}]
k^*	thermal conductivity ratio, k_s/k_l
L	length of enclosure [m]
Le	Lewis number, α_l/D_l
Nu	Nusselt number, see equation (13)
p	dimensionless pressure, $PL^2/(\rho_l\alpha_l^2)$
P	pressure [N m^{-2}]
Pr	Prandtl number, ν_l/α_l
R_s	stability number, $\beta_c C_E/\beta_T(T_w-T_E)$
Ra	Rayleigh number, $g\beta_l(T_w-T_E)L^3/(\nu_l\alpha_l)$
s	dimensionless liquid layer thickness, S/L
S	liquid layer thickness [m]
Ste	Stefan number, $c_l(T_w-T_E)/\Delta h$
t	time [s]
T	temperature [K]
u	dimensionless velocity, UL/α_l
U	velocity [m s^{-1}]
x	horizontal coordinate [m]
y	vertical coordinate [m].

Greek symbols

α	thermal diffusivity, $k/\rho c$ [m^2 s^{-1}]
α^*	thermal diffusivity ratio, α_s/α_l
β_c	concentration expansion coefficient
β_T	thermal expansion coefficient [K^{-1}]
γ	dimensionless slope of liquidus line, $\Gamma C_E/(T_w-T_E)$
Γ	slope of liquidus line [K]
η	dimensionless vertical coordinate, y/L
Θ	dimensionless temperature, $(T-T_E)/(T_w-T_E)$
κ	segregation coefficient, $C_{s,i}/C_{l,i}$
ν	kinematic viscosity [m^2 s^{-1}]
ξ	dimensionless horizontal coordinate, x/L
ρ	density [kg m^{-3}]
ρ^*	density ratio, ρ_s/ρ_l
τ	dimensionless time, $t\alpha_l/L^2$
Φ	dimensionless concentration, C/C_E.

Subscripts

E	eutectic
i	interface
in	initial
l	liquid
n	normal
p	pure
s	solid
w	left- or right-hand wall.

concentration boundary layer. Eventually, the melt water is mixed outwards into a series of horizontal layers separated by relatively thin interfaces. Again, such physical phenomena have not yet been predicted.

Of related interest are the experimental [11–14] and numerical [14–17] studies considering boundary layer flow during free convection melting of ice in saline water. Depending on the temperature and salinity of the ambient water, a number of distinctively different flow regimes have been observed. Typically, a relatively thin, upward flowing concentration boundary layer is established near the ice surface. The thermal boundary layer is, however, considerably thicker and the flow field can be upward or downward, depending on the magnitude and direction of the net buoyancy force at any location. The local melting rates can increase significantly in regions where the outer flow changes its direction resulting in complex shapes of the ice surface at later times. The numerical studies [14–17] are usually limited to specific flow regimes. Numerical solutions of the boundary layer equations have been obtained for the laminar [16, 17] and turbulent [14, 15] flow regimes. None of the previous investigations have considered variations in the interfacial concentrations and temperatures as well as heat conduction in the solid ice.

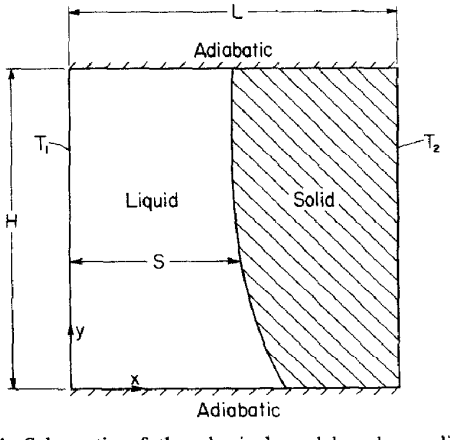

FIG. 1. Schematic of the physical model and coordinate system.

2. ANALYSIS

2.1. *Model equations*

The physical system considered in the present study is shown in Fig. 1. The vertical side walls of the enclosure are of height H and maintained at a temperature

T_w. The connecting horizontal walls of length L are considered adiabatic. The enclosure is occupied by vertical layers of a binary liquid (e.g. aqueous solution) and a solid consisting of one of the chemical species present in the liquid (e.g. ice). Initially the liquid layer is of thickness $S(y, t=0) = S_{in}$, the solid is of thickness $L - S(y, t=0)$, while both are at temperature T_w.

In the analysis, the flow is assumed to be laminar, incompressible and two-dimensional, and the Boussinesq approximation is invoked. The thermophysical properties are assumed constant, but may be different for the liquid and solid. Velocities at the solid/liquid interface due to density change upon melting as well as diffusion of species in the solid are neglected. With the foregoing assumptions, the governing equations for the liquid and solid can be written in dimensionless form (see Nomenclature) as:

liquid

$$\nabla \cdot \mathbf{u} = 0 \tag{1}$$

$$\frac{\partial \mathbf{u}}{\partial \tau} + (\mathbf{u} \cdot \nabla)\mathbf{u} = -\nabla p + Pr\,\nabla^2 \mathbf{u} + Ra\,Pr\,[\Theta + R_s \Phi]\mathbf{e}_\eta \tag{2}$$

$$\frac{\partial \Theta}{\partial \tau} + \mathbf{u} \cdot \nabla \Theta = \nabla^2 \Theta \tag{3}$$

$$\frac{\partial \Phi}{\partial \tau} + \mathbf{u} \cdot \nabla \Phi = \frac{1}{Le} \nabla^2 \Phi; \tag{4}$$

solid

$$\frac{\partial \Theta}{\partial \tau} = \alpha^* \nabla^2 \Theta. \tag{5}$$

The boundary and initial conditions for the present system are:

boundary conditions

$$\mathbf{u} = 0,\ \Theta = 1,\ \frac{\partial \Phi}{\partial \xi} = 0 \text{ at } \xi = 0,\ 0 \leqslant \eta \leqslant A$$

$$\mathbf{u} = 0,\ \Theta = 1,\ \frac{\partial \Phi}{\partial \xi} = 0 \text{ at } \xi = 1,\ 0 < \eta \leqslant A$$

$$\mathbf{u} = 0,\ \frac{\partial \Theta}{\partial \eta} = 0,\ \frac{\partial \Phi}{\partial \eta} = 0 \text{ at } \eta = 0, A,\ 0 \leqslant \xi \leqslant 1; \tag{6}$$

initial conditions

$$\mathbf{u} = 0,\quad \Theta = 1,\quad \Phi = \Phi_{in} \quad \text{for} \quad \tau \leqslant 0,$$
$$0 \leqslant \eta \leqslant A,\quad \xi < s(\eta, \tau)$$
$$\Theta = 1 \quad \text{for} \quad \tau \leqslant 0,\quad 0 \leqslant \eta \leqslant A,\quad s(\eta, \tau) < \xi \leqslant 1$$
$$s(\eta, \tau) = s_{in} \quad \text{for} \quad \tau \leqslant 0,\ 0 \leqslant \eta \leqslant A. \tag{7}$$

At the solid/liquid interface, $\xi = s(\eta, \tau)$, $0 \leqslant \eta \leqslant A$, the boundary conditions for $\mathbf{u}$, Θ and Φ are given by

$$\mathbf{u} = 0,\quad \Theta = \Theta_i,\quad \Phi = \Phi_i. \tag{8}$$

The interfacial temperature and concentration are directly related by the equilibrium phase diagram for a particular binary mixture. For the aqueous solution considered in the present study (see Section 3) the dependence of the melting temperature on concentration (i.e. liquidus curve) is well approximated by the linear relationship.

$$\Theta_i = \Theta_p + \gamma \Phi_{i,l} \tag{9}$$

where Θ_p and γ are the dimensionless melting temperature of the pure substance (i.e. for $\Phi = 0$) and slope of the liquidus curve, respectively. In addition, the concentrations of the liquid and solid at the interface are related by the constant segregation coefficient κ, i.e.

$$\kappa = \frac{\Phi_{i,s}}{\Phi_{i,l}}. \tag{10}$$

Finally, interfacial energy and mass balances yield, respectively, the following additional relationships:

$$k^*(\nabla \Theta \cdot \mathbf{n})_s - (\nabla \Theta \cdot \mathbf{n})_l = \frac{\rho^*}{Ste} v_n \tag{11}$$

$$-\frac{1}{Le}(\nabla \Phi \cdot \mathbf{n})_l = \rho^* \Phi_{i,l}(1-\kappa) v_n \tag{12}$$

where $\mathbf{n}$ is the unit vector normal to the interface and v_n is the velocity of this interface in the $\mathbf{n}$-direction.

In the above equations, the eutectic temperature, T_E, and concentration, C_E, as well as the wall temperature (T_w) have been utilized as reference values, so that the dimensionless quantities Θ and Φ are limited to values between zero and unity. The definitions of the other dimensionless quantities and parameters are provided in the Nomenclature.

The average heat transfer rates at the left- and right-hand wall will be presented in terms of the average Nusselt number defined as

$$Nu = \begin{cases} -\dfrac{1}{A}\displaystyle\int_0^A \frac{\partial \Theta}{\partial \xi} d\eta & \text{at } \xi = 0 \\ -\dfrac{1}{A}\displaystyle\int_0^A k^* \frac{\partial \Theta}{\partial \xi} d\eta & \text{at } \xi = 1 \end{cases}. \tag{13}$$

Note that with the above definition, the Nusselt number is based on the thermal conductivity of the liquid. For $k^* > 1$, this can lead to a Nusselt number above unity at the right-hand wall bounding the solid.

2.2. *Solution procedure*

The movement and the irregular shape of the solid/liquid interface considerably complicate the numerical solution of the coupled equations (1)–(12). In the present study, a modified form of the implicit/explicit approach proposed by Sparrow and co-workers [18, 19] is adopted for the treatment of the interface movement. The numerical solution proceeds through a series of small time intervals during which the solid/liquid interface is assumed to be fixed. For each such time interval, the field equations are solved by a

fully *implicit* solution scheme (without neglecting the unsteady terms) in the now fixed liquid and solid domains. The solution of the field equations provides the energy and mass fluxes at the interface after that time interval. The displacement of the interface can then be calculated *explicitly* (i.e. without iterations) from the interfacial energy or mass balances, equation (11) or (12), and new solution domains are generated for the next time step. Since the interface displacement is performed at the end of the time interval, the present approach avoids complications in the formulation of the numerical solution scheme for the field equations due to a moving grid system [19] as well as the iterative interaction of the temperature and concentration fields with the interface displacement [18]. The accuracy of this approach is demonstrated in the literature [18, 19]. In the following, the numerical procedures for solving the field equations during each time interval are outlined.

During phase change in binary mixtures, the local values of the interfacial temperature, Θ_i, and concentrations, $\Phi_{i,l}$ and $\Phi_{i,s}$, are not known *a priori*. Their values are, however, needed as boundary conditions for the solution of the field equations. This problem can be overcome by combining equations (11) and (12) and solving for the interfacial concentration, $\Phi_{i,l}$, which yields

$$\Phi_{i,l} = \frac{1}{Ste(1-\kappa)} \frac{-\frac{1}{Le}(\nabla\Phi\cdot\mathbf{n})_l}{[k^*(\nabla\Theta\cdot\mathbf{n})_s - (\nabla\Theta\cdot\mathbf{n})_l]}. \quad (14)$$

With the knowledge of $\Phi_{i,l}$, Θ_i and $\Phi_{i,s}$ can be calculated from the phase diagram relationships, equations (9) and (10). It can be seen from equation (14) that the interfacial temperature and concentrations depend on the heat and species fluxes at the interface. Obviously, these fluxes are, in turn, influenced by the values of Θ_i, $\Phi_{i,l}$ and $\Phi_{i,s}$. Hence, the interfacial temperature and concentrations must be obtained in an iterative manner, simultaneously with the solution of the field equations for each time interval. Since the ('implicit') solution scheme for the field equations is inherently of an iterative nature, this represented no major problem.

The field equations, equations (1)–(5), together with the boundary and initial conditions, equations (6)–(8), were solved utilizing a modified form of the control-volume based discretization scheme described in detail elsewhere [20, 21]. In this scheme, the field equations are integrated over discrete non-orthogonal control volumes. The additional terms due to the non-orthogonality of the grid are fully retained in the discretized equations. The modified algorithm is based on an implicit discretization scheme for the unsteady equations, without invoking the quasi-steady approximation [21]. Other details of the algorithm as well as the computational sequence are essentially the same as in ref. [20] and do not need to be repeated here.

The highly irregular shapes of the liquid and solid domains were accommodated in the calculations by using a non-orthogonal curvilinear grid. After each movement of the interface a new grid was algebraically generated utilizing a power-law clustering scheme [21]. This procedure provides a high concentration of nodal points near the vertical boundaries and the solid/liquid interface where velocity, thermal and concentration boundary layers need to be accurately resolved. The nodal points were only slightly skewed in the η-direction. In the calculations reported in the present study, grids of 26×26 nodal points were selected for the liquid and solid domains. It is realized that this relatively coarse grid might not be adequate to resolve all details of the double-diffusive flow structures in the liquid domain. The selected mesh size should only be viewed as a compromise between accuracy and computational cost. Additional tests for the accuracy of the numerical algorithm were performed for the limiting cases of melting of a pure substance [21] and thermal natural convection in a square enclosure [22] and good agreement with results reported in the literature was found.

A dimensionless time step of $\tau = 1 \times 10^{-5}$ was utilized to assure a very small interface displacement. For each time step, the iterations were terminated when the dependent variables agreed to four significant figures at each nodal point and the residual source of mass was less than 1×10^{-5}. For a total simulation time of approximately $\tau = 0.1$, the calculations required up to 5000 CPU s on a CYBER 205 digital computer.

3. EXPERIMENTS

3.1. *Test cell and instrumentation*

Experiments were performed in a well-insulated test cell of square cross section. The test cell had inside dimensions of 4.76 cm in height and width and 3.81 cm in depth. The horizontal bottom wall was constructed of a phenolic plate, while the top wall and the vertical front and back walls were made of Lexan. The two vertical side walls, which served as the heat source/sink, were multipass heat exchangers machined out of a copper plate. The heat exchangers were connected through a valve system to two constant temperature baths (Haake A82). Each heat exchanger contained three loops through which the flow rate could be controlled independently. The temperatures of each heat exchanger were measured with three thermocouples epoxied separately into small-diameter holes which were drilled close to the surface of the copper plate facing the fluid. In all experiments, the temperatures of each heat exchanger were uniform to within 0.1°C of the desired temperature. The entire test cell was insulated with 2.53 cm thick styrofoam.

Measurement of the temperature distribution inside the test cell was made with 33 thermocouples with a wire diameter of 0.127 mm. They were placed in three different rakes which were located at heights of 0.635, 2.38, and 4.125 cm measured from the bottom of

the test cell. The rakes were positioned such that the temperatures were measured along the vertical centerplane of the test cell. All thermocouples were calibrated with an accuracy of ± 0.1°C. The thermocouples were connected to a HP-85 data-logger and computer through which the temperatures could be measured and stored at preselected time intervals.

Qualitative observations of the density distribution and the flow structure in the liquid region were made using a shadowgraph system. The light source consisted of a collimated beam from a mercury-arc lamp. After passing through the test cell, the light was imaged on a white glass plate and photographed using a high-sensitivity film (Kodak Tmax 400). Flow visualization was also performed by injecting a Calcoid Blue ink solution in the liquid region. The ink solution had the same concentration as the initial concentration of the liquid (i.e. Φ_{in}). In the flow visualization experiments, the test cell was illuminated from the back through the Lexan windows using a white light source and a diffusing white glass plate. The ink solution was allowed to convect with the flow for some time and the entire test cell was then photographed from the front. It should be mentioned that in both, the shadowgraph and the flow visualization experiments, the solid region was masked with black paper. This was done to avoid reflections and scattering of the light by the solid and to increase the contrast between the liquid and solid regions (since the ice is transparent). During the time periods the photographs were taken, the insulation covering the liquid region was removed.

Concentration measurements were performed by withdrawing a few drops of the liquid with a hypodermic needle at the desired location in the test cell and analyzing them with a refractometer (Kernco). The refractometer was calibrated for the aqueous solution used in the present experiments (i.e. NH_4Cl–H_2O) with an accuracy of ± 0.2 wt.% (NH_4Cl).

3.2. *Test materials and conditions*

In all experiments, the solid consisted of ice formed from once distilled, degasified water, while the liquid was a solution of ammonium chloride (NH_4Cl) in water (H_2O). The equilibrium phase diagram of the NH_4Cl–H_2O system is of the eutectic type with a eutectic temperature, T_E, and concentration, C_E, of 257.75 K and 0.197 wt. fraction NH_4Cl, respectively [7, 23]. The mixture used in the present experiment was on the water-rich side of the eutectic point, so that the concentrations are conveniently expressed in terms of the wt. fraction NH_4Cl (i.e. $0 < C < 0.197$). On the water-rich side of the eutectic point, the liquidus line has a slope of approximately $\Gamma = -78.2$ K (with $T_p = 273.15$ K) and the segregation coefficient, κ, is equal to zero [7, 23].

A number of experiments with different initial and boundary conditions were performed [10]. For conciseness, only one case is presented in this paper. The experimental conditions together with the values of the dimensionless parameters for this experiment are summarized in Table 1. All properties were evaluated at the mean temperatures and concentrations. Some of the thermophysical property data for the NH_4Cl–H_2O solution at the present temperatures and concentrations are not readily available and were appropriately interpolated or estimated from the data provided in the literature [7, 23]. As shown in Table 1, the initial liquid concentration was equal to the eutectic concentration (i.e. $C_{in} = C_E = 0.197$), while both heat exchangers were maintained at 273.15 K (0°C). With these boundary and initial conditions and the relatively small concentration and temperature differences encountered in the experiment (i.e. less than 10 wt.% NH_4Cl and 8°C, respectively), the variations of the liquid density with concentration and temperature can be well approximated by linear functions (see Section 2.1).

3.3. *Experimental procedures*

In preparing for the experiment, the entire test cell was first filled with pure water. By lowering the right heat exchanger temperature below 273.15 K (0°C), a vertical ice layer was formed at that wall. During the solidification process, the liquid was continuously stirred to prevent the formation of small air pockets in the ice as well as to ensure a vertical and flat solid/liquid interface. When the desired thickness of the ice layer was reached, the remaining water was quickly syphoned out of the test cell. Then, the two heat exchangers were brought to the temperatures desired as the boundary (and initial) conditions (i.e. T_w). After the ice layer reached a uniform temperature, equal to T_w, an NH_4Cl–H_2O solution of the desired initial concentration ($C_{in} = C_E$) and temperature (T_w) was carefully syphoned into the test cell. At this time, the experiment started.

Due to the filling process, the zero velocity initial condition was not exactly realized. In addition, the temperatures and concentrations started changing during the filling period. Temperature measurements as well as visual observations indicated, however, that the filling process did not have a major influence on the experiments at later times. This was also confirmed

Table 1. Summary of experimental test conditions

T_1 (°C)	T_2 (°C)	C_{in}	S_{in}	A	Ra	R_s	Ste	Pr	Le	α^*	k^*	ρ^*	Θ_p	γ	κ
0	0	0.197	0.5	1.0	2.042×10^7	−17.88	0.157	9.45	157.47	8.723	4.68	0.878	1.0	−1.0	0.0

by repeating the same experiment several times using different filling procedures. Almost no differences in the temperatures and flow patterns were observed approximately 1 min after the filling process was completed. Finally, it should be mentioned that the various measurements (see above) were conducted in separate tests so that they did not interfere with each other.

4. RESULTS AND DISCUSSION

The numerical and experimental results for the conditions of Table 1 are shown in Figs. 2–7. The flow and heat and mass transfer patterns evident from both the numerical simulation and the experiment are described in the next subsection, which is followed by a comparison of the predictions with the data.

4.1. *Transport phenomena*

When the ice melts into the NH_4Cl–H_2O solution, the liquid adjacent to the solid/liquid interface becomes rich in water. This compositional change causes the density to decrease and the liquid confined in a thin concentration boundary layer rises up along the interface. Reaching the top of the enclosure, the water-rich liquid spreads horizontally and forms a layer above the fluid of the original composition. Since the ice and the liquid at the interface are in local equilibrium, the compositional change also causes the temperatures of the interface to decrease according to the melting point depression curve, equation (9). With the interfacial temperatures being below the right-hand wall temperature (i.e. 0°C), heat is conducted through the solid ice, towards the interface. On the liquid side, the interfacial temperature depression results in an increase of the density of the fluid adjacent to the interface. Inside the concentration boundary layer, the density decrease due to the compositional change exceeds the density increase due to the lower temperature. In the uncontaminated fluid of the original composition, however, the interfacial temperature decrease causes thermal natural convection to develop. In the region outside the concentration boundary layer, the liquid flows downwards in a thermal boundary layer. The thermal boundary layer is much thicker than the concentration boundary layer, because of the large Lewis number ($Le \approx 157$). Since the left-hand wall is above the interface temperature, the liquid flows upwards at this wall and a clockwise rotating convection cell is established in the uncontaminated fluid. Note that all of the above heat convection and conduction processes are solely due to the melting temperature depression caused by the compositional changes at the solid/liquid interface, while, both the left- and right-hand walls are kept at the same temperature (i.e. 0°C).

The detailed time evolution of these transport processes can be seen from Figs. 2 to 4. At 2 min into the experiment ($\tau = 0.697 \times 10^{-2}$), the water-rich, horizontal layer at the top of the liquid region has reached a thickness of approximately 13% of the total height of the test cell. This layer is stably stratified with the concentration (and density) decreasing towards the top (Fig. 2(c)). The lines of constant concentration are tilted downwards away from the left-hand wall (see also Figs. 3(c) and 4(c)), because the horizontal temperature drop between the left-hand wall and the interface results in a slight increase in the density of the stratified fluid towards the interface. Besides the spreading of the fluid arriving from the concentration boundary layer, the flow in the top layer is relatively weak (Fig. 2(a)), indicating that the thermal buoyancy forces are not able to offset the stable stratification due to concentration. Accordingly, the isotherms are relatively straight (Fig. 2(b)) and heat transfer is mostly by conduction. As can be seen from the predicted streamlines (Fig. 2(a)), the flow in the thin concentration boundary layer along the solid/liquid interface (Fig. 2(c)) is upwards, carrying fluid, which is contaminated by the melt water, into the top layer. Most of the fluid does not reach the top of the enclosure but spreads horizontally at a height in the top layer where its density is equal to the surrounding density (see also Figs. 3(a) and 4(a)). This indicates that the composition of the fluid in the concentration boundary layer is not uniform. The fluid closest to the interface has the highest water content and, therefore, rises to the top of the enclosure, while the fluid from the outer regions of the concentration boundary layer is less diluted and reaches its equilibrium height at a lower level. The remaining liquid below the top layer is completely uncontaminated by the melt water and is compositionally homogeneous (Fig. 2(c)). Thermal natural convection in the uncontaminated liquid is relatively strong. Accordingly, the isotherms (Fig. 2(b)) are clustered in the thermal boundary layers adjacent to the left-hand wall and the interface is almost horizontal in the core of the convection cell. Note that some heat is conducted from the uncontaminated region into the top layer. In the solid, the isotherms (Fig. 2(b)) are not completely straight and vertical, indicating that the solid/liquid interface is not isothermal (see below for a discussion of the interfacial temperature and concentration distributions).

As shown in Figs. 3(c) and 4(c), the vertical extent of the stratified top layer increases continuously with time at the expense of the uncontaminated fluid region. The fluid flow (Figs. 3(a) and (4)) and heat transfer (Figs. 3(b) and 4(b)) patterns remain qualitatively the same as described above for $\tau = 0.697 \times 10^{-2}$ (2 min). At $\tau = 10.455 \times 10^{-2}$ (30 min) almost the entire liquid is compositionally stratified. Due to the decreasing height of the uncontaminated layer, thermal natural convection in this layer becomes weaker with increasing time. On the other hand, the intensity of the natural convection flow in the stratified region gradually increases. This indicates that at later times, the thermal buoyancy forces are able to break up some of the stratification due to concentration and initiate thermal natural con-

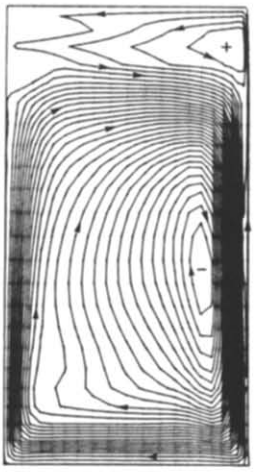

(a)

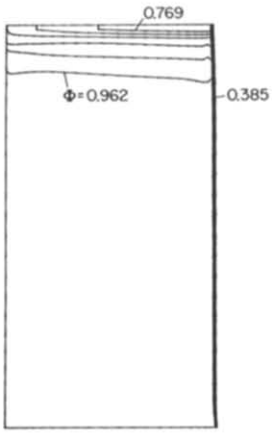

(c)

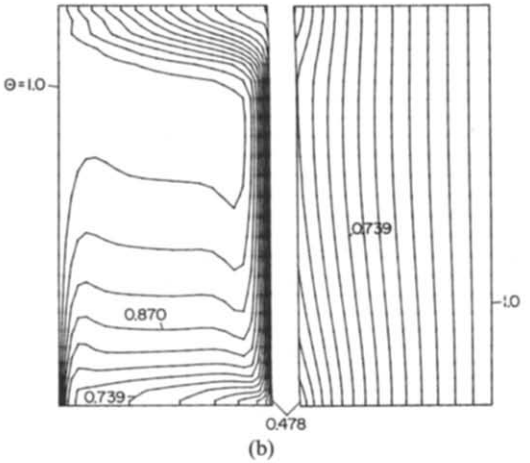

(b)

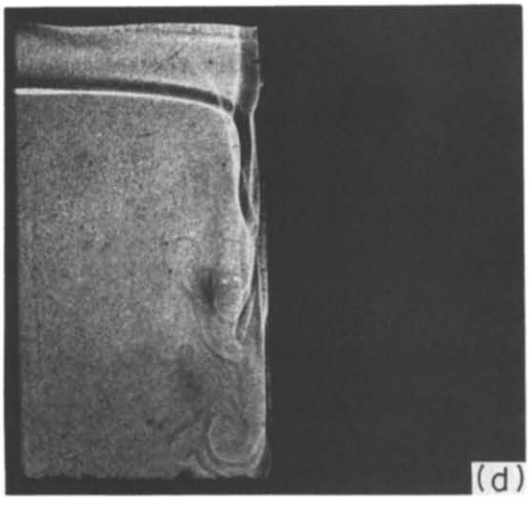

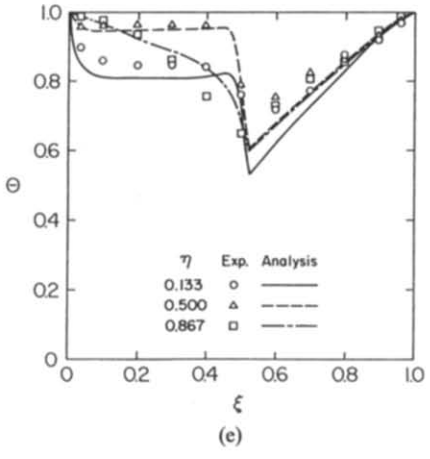

(e)

FIG. 2. Measured and predicted results at $\tau = 0.697 \times 10^{-2}$ ($t = 2$ min): (a) streamlines ($\psi_{min} = -30.58$, $\psi_{max} = 5.42$, equal increments); (b) isotherms (equal increments) (the left-hand panel represents the liquid and the right the ice); (c) concentration isoplets (equal increments); (d) shadowgraph; (e) temperature profiles.

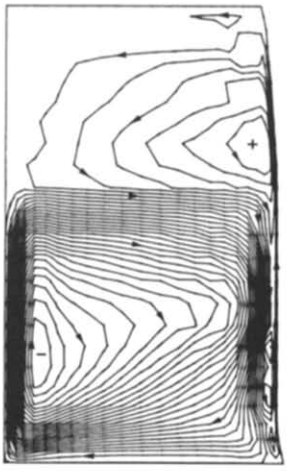

(a)

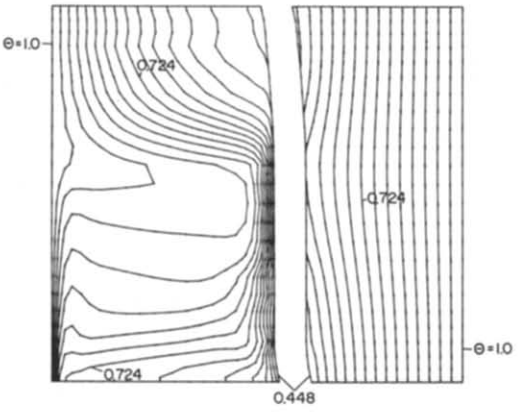

(b)

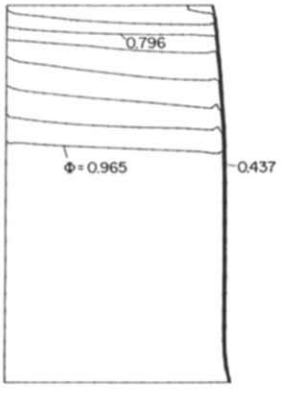

(c)

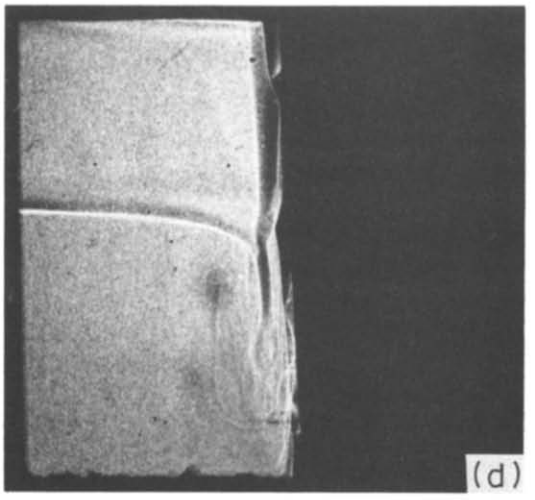

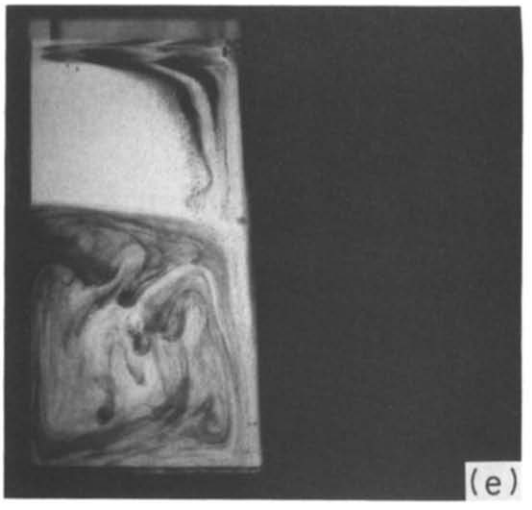

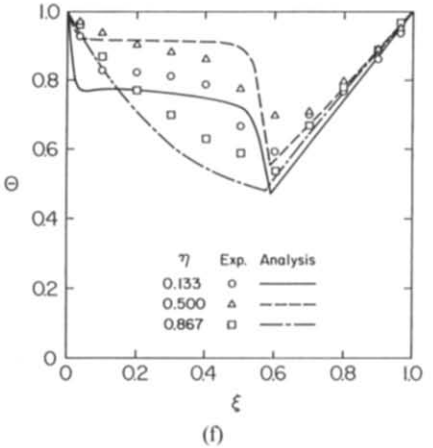

(f)

FIG. 3. Measured and predicted results at $\tau = 3.485 \times 10^{-2}$ ($t = 10$ min); (a) streamlines ($\psi_{min} = -20.54$, $\psi_{max} = 5.45$, equal increments); (b) isotherms (equal increments) (the left-hand panel represents the liquid and the right the ice); (c) concentration isoplets (equal increments); (d) shadowgraph; (e) flow visualization; (f) temperature profiles.

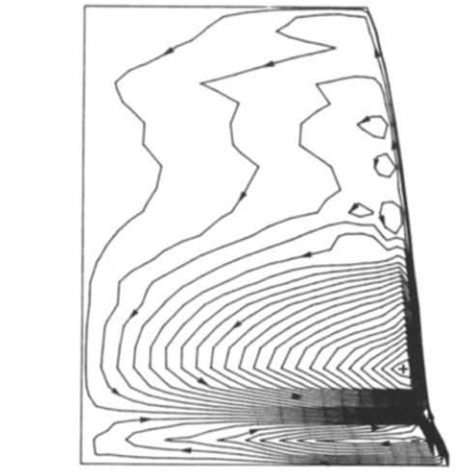

(a)

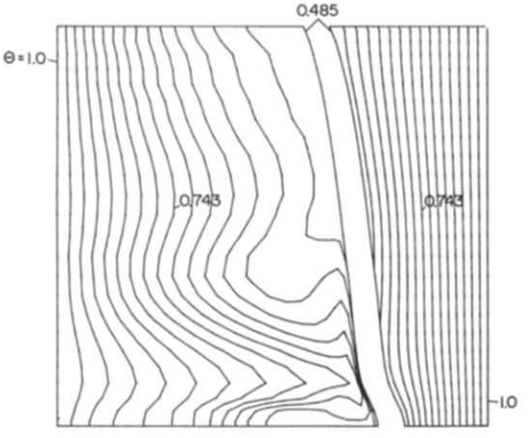

(b)

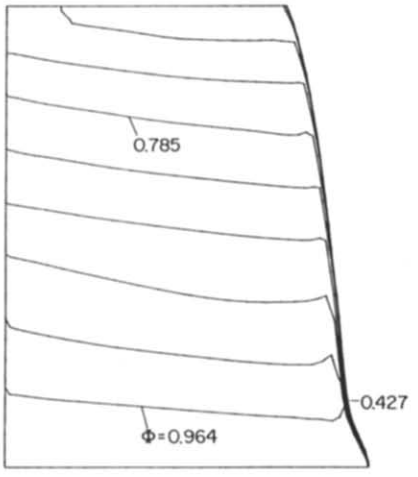

(c)

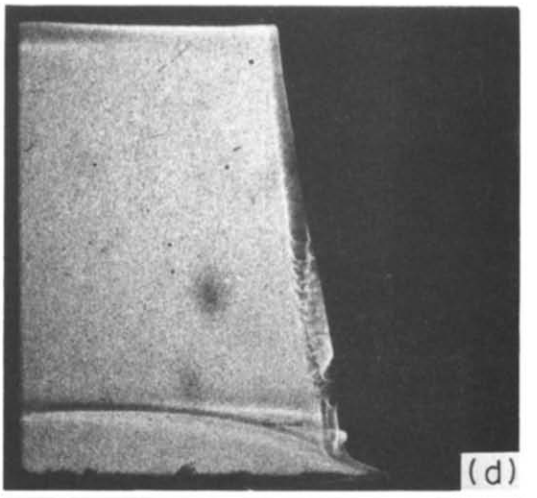

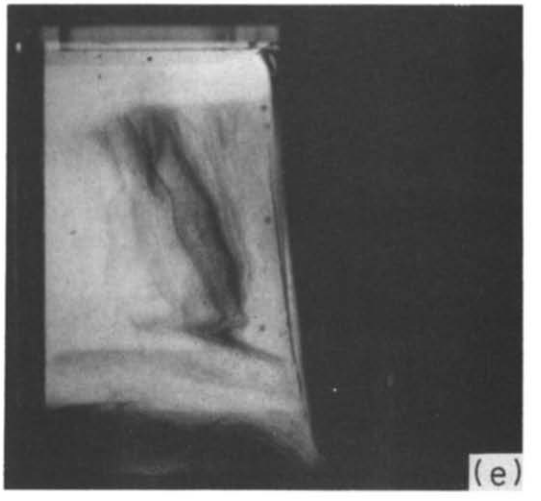

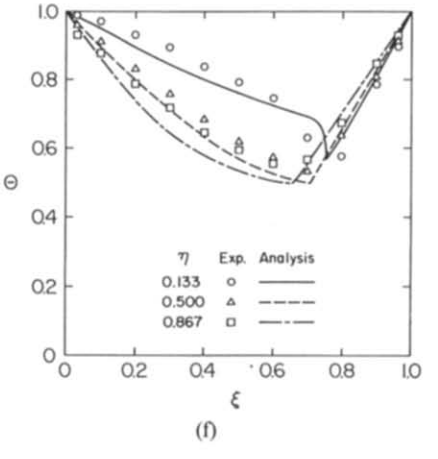

(f)

FIG. 4. Measured and predicted results at $\tau = 10.455 \times 10^{-2}$ ($t = 30$ min): (a) streamlines ($\psi_{min} = -6.16$, $\psi_{max} = 14.70$, equal increments); (b) isotherms (equal increments) (the left-hand panel represents the liquid and the right the ice); (c) concentration isoplets (equal increments); (d) shadowgraph; (e) flow visualization; (f) temperature profiles.

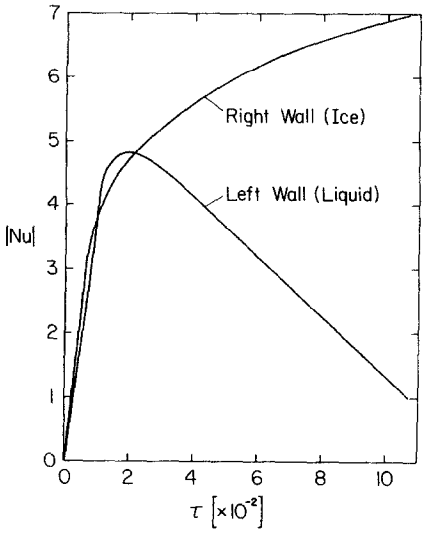

FIG. 5. Time evolution of the predicted Nusselt numbers at the vertical side walls.

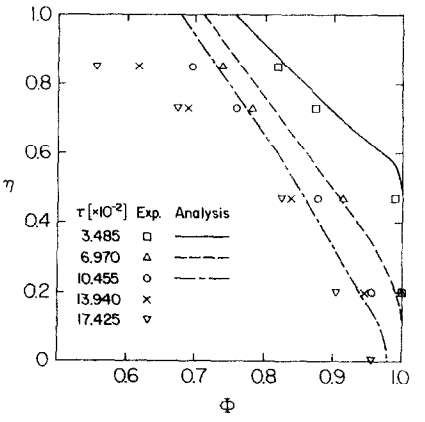

FIG. 7. Comparison of predicted and measured concentration profiles.

vection. As can be seen from the predicted results at $\tau = 10.455 \times 10^{-2}$ (30 min), most of this flow is, however, confined to the lower portion of the stratified layer, while the heat transfer in the upper half of the enclosure is dominated by conduction.

The time evolution of the heat transfer patterns is further delineated by a plot of the average Nusselt numbers at the left- and right-hand walls, which is shown in Fig. 5. During the first 5 min (until $\tau \approx 1.7 \times 10^{-2}$), the heat transfer rates at both walls increase sharply due to the decrease in the interface temperature and the development of the flow. At later times, however, the Nusselt number at the left-hand wall gradually decreases. This can be explained by the fact that the extent of the stably stratified region increases, while the intensity of the convective flow in the uncontaminated liquid region decreases, both of which tend to suppress the heat transfer across the liquid. On the other hand, the Nusselt number at the right-hand wall continues to increase because of the decreasing thickness of the ice layer.

As discussed previously, the interfacial temperatures and concentrations as well as the local melting rates are directly determined by the heat and mass transfer rates at the interface. A plot of the interfacial temperature and concentration distributions is shown for various times in Fig. 6. It can be seen that at all times there exists a maximum (minimum) in the interfacial temperature (concentration) at the vertical location which separates the strongly convecting, uncontaminated liquid layer at the bottom from the stably stratified top layer, indicating that at this location, the ratio of the concentration and temperature gradients, given by equation (14), is lowest. The interfacial temperature (concentration) decreases (increases) towards the top and bottom of the enclosure. Since the stratified top layer continues to grow, the location of the interfacial temperature (concentration) maximum (minimum) moves gradually towards the bottom of the enclosure.

These variations in the temperature and concentration gradients normal to the interface are also reflected by the local melting rates. Due to the presence of a thermal boundary layer along the interface in the uncontaminated bottom layer, the temperature gradients are large in this region (Figs. 2(b)–4(b)). On the other hand, the temperature gradients at the interface in the stratified top layer are relatively small. Consequently, the interface moves faster in the bottom layer than in the stratified region (equation (11)). Since the extent of the stratified region continuously increases, the effects of a higher melting rate in the bottom convection layer are smeared. out. After some time, the solid/liquid interface becomes curved with the horizontal extent of the liquid region smoothly increasing from the top. The above discussion does, however, not explain the curvature of the interface

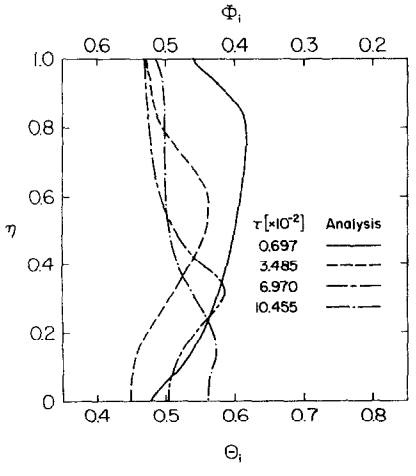

FIG. 6. Predicted interfacial temperature and concentration distributions.

within the uncontaminated layer, close to the bottom of the enclosure (Figs. 3 and 4). This region is characterized by the development of the concentration boundary layer along the interface in which the flow is upward. Its thickness increases from zero at $\eta = 0$ to its maximum value at the top of the bottom convecting layer (Figs. 2(c)–4(c)). Accordingly, the concentration gradients normal to the interface sharply increase towards $\eta = 0$. In view of equation (12), this results in a simultaneous increase in the local melting rate with decreasing η. Due to computer time limitations, the numerical simulation of the experiment was terminated at $\tau = 10.455 \times 10^{-2}$ (30 min). It was observed [10], however, that at later times, the melting rates continued to be very high at the bottom of the enclosure, while very little melting occurred over the remaining parts of the interface. After a long time (~ 2 h), the ice at the bottom third of the enclosure was completely melted, leaving a small ice layer at the upper part of the right-hand wall. As expected, the system reaches a steady state (after approximately 5 h), which is characterized by an isothermal (at 0°C) and quiescent liquid having a uniform composition, $\Phi = 0.5$ [10].

4.2. *Comparison of predictions with data*

The extent of the stably stratified top region was experimentally determined using the shadowgraph system. The photographs of the shadowgraph images are shown for $\tau = 0.697 \times 10^{-2}$ (2 min), 3.485×10^{-2} (10 min), and 10.455×10^{-2} (30 min) in Figs. 2(d), 3(d), and 4(d), respectively. It can be seen that the stratified top layer is separated by a sharp ('double-diffusive') interface from the uncontaminated bottom layer. The development of such sharp interfaces is well known for heating (or cooling) a stable concentration gradient from the side [3, 5]. It depends explicitly on the different diffusivities for heat and mass and is caused by the thermal natural convection flow in the bottom layer. Because the liquid effectively retains its (original) composition, the flow is constrained by the concentration (density) stratification and a definite interface above the convecting layer is formed. As mentioned above, the thermal buoyancy forces in the experiment are not strong enough to establish such convective layers in the stratified region in the upper part of the enclosure. At all times, the location and tilt of the double-diffusive interface coincides well with the predicted upper boundary of the uncontaminated bottom layer. Small differences in the heights of the bottom layer can possibly be attributed to the initial problems with the filling of the liquid region with the solution as discussed earlier. In addition, the neglect of three-dimensional effects in the numerical simulation may result in an underprediction of the melting rates and, thus, the growth of the stratified region.

The photographs of the flow visualization experiment are shown for $\tau = 3.485 \times 10^{-2}$ (10 min) and 10.455×10^{-2} (30 min) in Figs. 3(e) and 4(e), respectively. In general, the agreement between the predicted streamlines (Figs. 3(a) and 4(a)) and the flow patterns revealed by the flow visualization experiment is good. Because the dye had the same composition as the initial concentration of the liquid (i.e. Φ_{in}), most of it is confined to the uncontaminated bottom layer and does not mix with the diluted liquid. Only a small amount of dye is carried through the concentration boundary layer into the stratified region, where it slowly spreads out. The slow spreading of the flow in the stratified layer can be seen from a comparison of the dye patterns in Figs. 3(e) and 4(e), and is in good agreement with the results of the numerical simulation. The flow visualization also confirms the existence of a strong, clockwise rotating convection cell in the bottom layer. Figure 3(e) clearly shows that this convection cell does not extend entirely towards the solid/liquid interface, but is bounded by the (dye free) concentration boundary layer adjacent to the interface. Since the size of the bottom layer decreases with time, the dye becomes more concentrated and diffused so that at $\tau = 10.455 \times 10^{-2}$ (30 min) the bottom layer appears very dark (Fig. 4(e)).

Quantitative comparison between the measured and predicted temperatures are shown in Figs. 2(e), 3(f), and 4(f). As mentioned earlier, temperature measurements were taken at three different heights in the test cell. At all times and heights, the temperature profiles show sharp discontinuities at the solid/liquid interface, which is due to the latent heat absorption during melting. The profiles in the stratified layer as well as in the solid are relatively straight, indicating that the heat transfer is by conduction. On the other hand, the profiles in the convecting bottom layer show sharp gradients at the left-hand wall and the solid/liquid interface, while the core region is characterized by almost horizontal profiles. This is typical for natural convection in a vertical cavity of the same aspect ratio as the bottom layer. It can be seen that the measured and predicted temperatures agree qualitatively well. Some of the discrepancies may be attributed to heat gains through the bottom and top walls of the test cell as well as uncertainties in the thermocouple locations and readings (see above). In addition, uncertainties and variations in the values of the thermophysical properties, numerical inaccuracies (considering the relatively coarse mesh in the liquid region), and possible three-dimensional effects may be the cause of some deficiencies in the numerical simulation.

A quantitative comparison between measured and predicted concentrations at various times is presented in Fig. 7. Concentration measurements were made at several heights in the vertical centerplane of the test cell, midway between the left-hand wall and the solid/liquid interface. The agreement between the measured and predicted concentrations is relatively good. Most of the discrepancies can be explained by the inaccuracies of the refractometer (± 0.2 wt.% NH_4Cl) and the uncertainties in the location of the tip of the hypodermic needle. Shown in Fig. 7 are also con-

centration measurements taken at two different times after the termination of the numerical simulation (i.e. $t = 40$ and 50 min). It can be seen that the concentrations near the top of the test cell continue to decrease, while the concentration gradient across the height of the enclosure becomes steeper. Note that at 50 min, the liquid at the very bottom of the test cell is slightly diluted by the melt water (i.e. $\Phi \approx 0.96$ at $\eta \approx 0$).

5. CONCLUSIONS

A combined numerical and experimental study of double-diffusive convection due to melting of ice into an aqueous solution is performed. The dimensionless equations are solved utilizing an algorithm which is based on curvilinear, non-orthogonal control volumes. The model is successfully validated through an experiment conducted in a vertical square cavity initially containing vertical layers of ice and an ammonium chloride–water (NH_4Cl–H_2O) solution. A discussion of the deficiencies in the model and the experimental setup as well as of the physical phenomena occurring in the experiment is presented.

For the first time, it has been possible to predict the two-dimensional, transient transport phenomena during melting in a binary system. This is particularly noteworthy in view of the fact that the present system is characterized by relatively complicated double-diffusive convection and melting processes. The numerical simulation has revealed a number of interesting phenomena that have not been considered in the past. It is found that the convection processes in the liquid cause considerable variations in the interfacial temperature and concentration distributions. Furthermore, the numerical predictions provide insight into the detailed physical processes leading to the observed variations in the local melting rates over the height of the solid layer. Quantitative results are also obtained for the heat conduction in the solid and the time evolution of the heat transfer rates at the vertical side walls.

Although only a single test case is included in this paper, other experiments [5, 6, 8, 10–14] show that the results and conclusions presented are of a more general nature, applicable to many situations involving melting of a vertical ice layer into a binary mixture. The present work also represents a first step towards numerically simulating even more complicated melting processes in binary mixtures. For example, the transport phenomena are expected to be completely different for other configurations of the solid and liquid layers. Although it is theoretically possible to utilize the present model and algorithm for more complicated melting processes, such numerical simulations are expected to require very large computational resources (i.e. due to the fine grid and small time steps necessary). Consequently, research is needed to develop more accurate, stable, and efficient numerical algorithms. In addition, modeling of property variations and three-dimensional effects need more research attention.

Acknowledgements—The work reported in this paper was supported, in part, by the National Science Foundation under Grant No. CBT-8313573. Computer facilities were made available by Purdue University Computing Center.

REFERENCES

1. K. M. Fisher, The effects of fluid flow on the solidification of industrial castings and ingots, *Physico-Chem. Hydrodyn.* **2**, 311–326 (1981).
2. S. M. Pimputkar and S. Ostrach, Convective effects in crystals growth from melt, *J. Crystal Growth* **55**, 614–646 (1981).
3. H. E. Huppert and R. S. J. Sparks, Double-diffusive convection due to crystallization in magmas, *Ann. Rev. Earth Planet. Sci.* **12**, 11–37 (1984).
4. C. F. Chen and J. S. Turner, Crystallization in a double-diffusive system, *J. Geophys. Res.* **85**, 2573–2593 (1980).
5. J. S. Turner and L. B. Gustafson, Fluid motions and compositional gradients produced by crystallization or melting at vertical boundaries, *J. Volcanology Geothermal Res.* **11**, 93–125 (1981).
6. H. E. Huppert and J. S. Turner, Ice blocks melting into a salinity gradient, *J. Fluid Mech.* **100**, 367–384 (1980).
7. S. M. Copley, A. F. Giamei, S. M. Johnson and M. F. Hornbecker, The origin of freckles in unidirectionally solidified castings, *Metall. Trans.* **1**, 2193–2204 (1970).
8. H. E. Huppert and J. S. Turner, Double-diffusive convection, *J. Fluid Mech.* **106**, 299–329 (1981).
9. C. F. Chen and D. H. Johnson, Double-diffusive convection: a report on an Engineering Foundation conference, *J. Fluid Mech.* **138**, 405–416 (1984).
10. C. Beckermann, Melting and solidification in binary systems with double-diffusive convection in the melt, Ph.D. Thesis, Purdue University (1987).
11. V. P. Carey and B. Gebhart, Transport near a vertical ice surface melting in saline water: experiments at low salinities. *J. Fluid Mech.* **117**, 403–423 (1982).
12. B. Sammakia and B. Gebhart, Transport adjacent to ice surfaces melting in saline water: visualization experiments, *Int. Commun. Heat Mass Transfer* **11**, 25–34 (1984).
13. R. S. Johnson and J. C. Mollendorf, Transport from a vertical ice surface melting in saline water, *Int. J. Heat Mass Transfer* **27**, 1928–1932 (1984).
14. E. G. Josberger and S. Martin, A laboratory and theoretical study of the boundary layer adjacent to a vertical melting ice wall in salt water, *J. Fluid Mech.* **111**, 439–473 (1981).
15. V. P. Carey and B. Gebhart, Transport near a vertical ice surface melting in saline water: some numerical calculations, *J. Fluid Mech.* **117**, 379–402 (1982).
16. E. Marschall, Free convection melting of glacial ice in saline water, *Lett. Heat Mass Transfer* **4**, 381–384 (1977).
17. A. Davies and E. Marschall, Heat and mass transfer during mixed convection melting of glacial ice in saline water, *Int. Commun. Heat Mass Transfer* **11**, 199–208 (1984).
18. E. M. Sparrow and W. Chuck, An implicit/explicit numerical solution scheme for phase-change problems, *Numer. Heat Transfer* **7**, 1–15 (1984).
19. E. M. Sparrow and Y. Ohkubo, Numerical analysis of two-dimensional transient freezing including solid-phase and tube-wall conduction and liquid-phase natural convection, *Numer. Heat Transfer* **9**, 59–77 (1986).
20. C. F. Hsu, A curvilinear-coordinate method for momentum, heat, and mass transfer in domains of irregular

geometry, Ph.D. Thesis, University of Minnesota (1982).
21. B. W. Webb and R. Viskanta, Analysis of heat transfer during melting of a pure metal from an isothermal vertical wall, *Numer. Heat Transfer* **9**, 539–558 (1986).
22. G. deVahl Davis and I. P. Jones, Natural convection in a square cavity: a comparison exercise, *Int. J. Numer. Meth. Fluids* **3**, 227–248 (1983).
23. *International Critical Tables of Numerical Data, Physics, Chemistry and Technology*, Vol. 3, p. 60 and Vol. 4, p. 218 (1928).

CONVECTION A DOUBLE DIFFUSION DUE A LA FUSION

Résumé—On étudie numériquement et expérimentalement la fusion d'une couche de glace verticale dans une solution aqueuse de chlorure d'ammonium à l'intérieur d'une cavité carrée. Les équations sont résolues avec un algorithme basé sur des volumes de contrôle curvilinéaires et non orthogonaux. Ces résultats numériques sont validés par la méthode d'ombre pour visualiser, par les mesures de température et de concentration. On trouve que le mécanisme de fusion induit des gradients de température et de concentration dans le liquide intialement homogène. A cause de la nature doublement diffusive du système, il se développe une stratification stable en concentration au dessus d'une couche de liquide non contaminée avec forte convection. On montre que les mécanismes de convection à double diffusion cause des variations considérables dans les vitesses locales de fusion et distributions interfaciales de température et de concentration. Les flux thermiques sur les parois verticales de la cavité et la conduction thermique dans la région solide reflètent fortement l'évolution dans le temps des phénomènes de convection doublement diffusifs induits par la fusion.

TEMPERATUR- UND KONZENTRATIONSGETRIEBENE KONVEKTION BEIM SCHMELZEN

Zusammenfassung—Es wird eine kombinierte numerische und experimentelle Studie zum Schmelzen einer vertikalen Eisschicht in einer Ammoniumchlorid–Wasser Lösung in einem quadratischen Hohlraum vorgestellt. Die Bilanz-Gleichungen werden unter Benutzung eines Algorithmus' gelöst, der auf körperkonturangepaßten, nicht orthogonalen Kontrollvolumina basiert. Die numerischen Ergebnisse werden durch Schattenaufnahmen, Sichtbarmachung der Strömung, Temperatur- und Konzentrationsmessungen bestätigt. Es zeigte sich, daß der Schmelzprozess Temperatur- und Konzentrationsgradienten in der anfangs homogenen Flüssigkeit hervorruft. Da das System temperatur- und konzentrationsgetriebene Konvektion aufweist, ergibt sich eine stabile Konzentrationsschichtung über einer Schicht stark zirkulierender, nicht verunreinigter Flüssigkeit. Abschließend wird gezeigt, daß der Konvektionsprozess erhebliche Schwankungen der lokalen Schmelzgeschwindigkeit und der Temperatur- und Konzentrationsverteilung an der Grenzschicht hervorruft. Der Wärmeübergang an den vertikalen Wänden des Hohlraumes und die Wärmeleitung im Festkörper werden sehr stark von der zeitlichen Entwicklung der Konvektionsphänomene beeinflußt, die vom Schmelzvorgang hervorgerufen werden.

СОВМЕСТНАЯ ТЕПЛОВАЯ И КОНЦЕНТРАЦИОННАЯ КОНВЕКЦИЯ ПРИ ПЛАВЛЕНИИ

Аннотация—Численно и экспериментально исследуется таяние вертикального слоя льда в водном растворе хлористого аммония внутри квадратной полости. Для решения определяющих уравнений используется алгоритм, основанный на методе криволинейного неортогонального контрольного объема. Теневая фотография, визуализация потока, а также измерения температуры и концентрации полностью подтверждают полученные численные результаты. Найдено, что в процессе плавления в однородной вначале жидкости возникают градиенты температуры и концентрации. Совместная тепловая и концентрационная конвекция в системе приводят к развитию устойчивой концентрационной стратификации над слоем чистой жидкости, находящейся в состоянии интенсивного движения. Показано, что процесс совместной конвекции вызывает значительные изменения локальных скоростей таяния и распределений температуры и концентрации на границе раздела фаз. Интенсивность переноса тепла у вертикальных стенок полости и передача тепла теплопроводностью в твердой фазе сильно зависят от развития во времени совместной тепловой и концентрационной конвекции при плавлении.